Investigation of spectral properties and lateral confinement of THz waves on a metal-rod-array-based photonic crystal waveguide

doi: 10.1364/OE.26.015570

Research Article | Vol. 26, No. 12 | 11 Jun 2018 | OPTICS EXPRESS 15570
Optics EXPRESS

Investigation of spectral properties and lateral confinement of THz waves on a metal-rod-array-based photonic crystal waveguide

Borwen You,[1] Dejun Liu,[1] Toshiaki Hattori,[1] Tze-An Liu,[2] and Ja-Yu Lu[3,*]

[1]*Department of Applied Physics, University of Tsukuba, Tennodai 1-1-1, Tsukuba, Ibaraki 305-8573, Japan*
[2]*Center for Measurement Standards, Industrial Technology Research Institute, Hsinchu 30011, Taiwan*
[3]*Department of Photonics, National Cheng Kung University, No. 1 University Road, Tainan 70101, Taiwan*
**jayu@mail.ncku.edu.tw*

Abstract: Terahertz (THz) waves laterally confined in a 1 mm-thick microstructured planar waveguide are demonstrated on a free-standing metal rod array (MRA), and one apparent rejection band of a transmission spectrum, resembling the bandgap of a photonic crystal, is found in 0.1–0.6 THz. The visibility of the photonic bandgap in the spectral width and power distinction can be manipulated by changing the MRA geometry parameters, including the rod diameter, the interspace between adjacent rods, and the propagation length based on an interactive MRA-layer number. THz transmission ratio enhanced by a large interactive length is verified in 30 MRA layers due to the longitudinally resonant guidance of transverse-magnetic-polarized waveguide modes along the MRA length, which is critical to the interspace width of adjacent rods and the metal coating of the rod surface. For an MRA with respective rod diameter and interspace dimensions of about 0.16 and 0.26 mm, the highest transmission of the guided resonant THz waves are performed at 0.505–0.512 THz frequency with strong confinement on the metal rod tips and a low scattering loss of 0.003 cm^{-1}.

OCIS codes: (050.5298) Photonic crystals; (230.7400) Waveguides, slab; (300.6495) Spectroscopy, terahertz.

References and links

1. E. Kuramochi, "Manipulating and trapping light with photonic crystals from fundamental studies to practical applications," J. Mater. Chem. C Mater. Opt. Electron. Devices **4**(47), 11032–11049 (2016).
2. R. Halir, P. J. Bock, P. Cheben, A. Ortega-Moñux, C. Alonso-Ramos, J. H. Schmid, J. Lapointe, D.-X. Xu, J. G. Wangüemert-Pérez, Í. Molina-Fernández, and S. Janz, "Waveguide sub-wavelength structures: a review of principles and applications," Laser Photonics Rev. **9**(1), 25–49 (2015).
3. E. Özbay, E. Michel, G. Tuttle, R. Biswas, K. M. Ho, J. Bostak, and D. M. Bloom, "Terahertz spectroscopy of three-dimensional photonic band-gap crystals," Opt. Lett. **19**(15), 1155–1157 (1994).
4. J.-M. Lourtioz, H. Benisty, A. Chelnokov, S. David, and S. Olivier, "Photonic crystals and the real world of optical telecommunications," Ann. Telecommun. **58**, 1197–1237 (2003).
5. F. Chiavaioli, F. Baldini, S. Tombelli, C. Trono, and A. Giannetti, "Biosensing with optical fiber gratings," Nanophotonics **6**(4), 663–679 (2017).
6. M. Walther, B. M. Fischer, and P. U. Jepsen, "Noncovalent intermolecular forces in polycrystalline and amorphous saccharides in the far infrared," Chem. Phys. **288**(2-3), 261–268 (2003).
7. T.-I. Jeon and D. Grischkowsky, "THz Zenneck surface wave (THz surface plasmon) propagation on a metal sheet," Appl. Phys. Lett. **88**(6), 061113 (2006).
8. S. A. Maier, S. R. Andrews, L. Martín-Moreno, and F. J. García-Vidal, "Terahertz surface plasmon-polariton propagation and focusing on periodically corrugated metal wires," Phys. Rev. Lett. **97**(17), 176805 (2006).
9. M. Gong, T.-I. Jeon, and D. Grischkowsky, "THz surface wave collapse on coated metal surfaces," Opt. Express **17**(19), 17088–17101 (2009).
10. H. Zhan, R. Mendis, and D. M. Mittleman, "Characterization of the terahertz near-field output of parallel-plate waveguides," J. Opt. Soc. Am. B **28**(3), 558–566 (2011).
11. B. Ng, J. Wu, S. M. Hanham, A. I. Fernández-Domínguez, N. Klein, Y. F. Liew, M. B. H. Breese, M. Hong, and S. A. Maier, "Spoof plasmon surfaces: a novel platform for THz sensing," Adv. Opt. Mater. **1**(8), 543–548 (2013).

#326612 https://doi.org/10.1364/OE.26.015570
Journal © 2018 Received 21 Mar 2018; revised 7 May 2018; accepted 21 May 2018; published 6 Jun 2018

Optics EXPRESS

12. B. Ng, S. M. Hanham, J. Wu, A. I. Fernández-Domínguez, N. Klein, Y. F. Liew, M. B. H. Breese, M. Hong, and S. A. Maier, "Broadband terahertz sensing on spoof plasmon surfaces," ACS Photonics **1**(10), 1059–1067 (2014).
13. B. You, C.-C. Peng, J.-S. Jhang, H.-H. Chen, C.-P. Yu, W.-C. Lai, T.-A. Liu, J.-L. Peng, and J.-Y. Lu, "Terahertz plasmonic waveguide based on metal rod arrays for nanofilm sensing," Opt. Express **22**(9), 11340–11350 (2014).
14. B. You, C.-Y. Chen, C.-P. Yu, T.-A. Liu, T. Hattori, and J.-Y. Lu, "Terahertz artificial material based on integrated metal-rod-array for phase sensitive fluid detection," Opt. Express **25**(8), 8571–8583 (2017).
15. D. R. Smith, S. Schultz, N. Kroll, M. Sigalas, K. M. Ho, and C. M. Soukoulis, "Experimental and theoretical results for a two-dimensional metal photonic band-gap cavity," Appl. Phys. Lett. **65**(5), 645–647 (1994).
16. N. A. Nicorovici, R. C. McPhedran, and L. C. Botten, "Photonic band gaps for arrays of perfectly conducting cylinders," Phys. Rev. E Stat. Phys. Plasmas Fluids Relat. Interdiscip. Topics **52**(1), 1135–1145 (1995).
17. S.-W. Wang, W. Lu, X.-S. Chen, Z.-F. Li, X.-C. Shen, and W. Wen, "Two-dimensional photonic crystal at THz frequencies constructed by metal-coated cylinders," J. Appl. Phys. **93**(11), 9401–9403 (2003).
18. B. Reinhard, G. Torosyan, and R. Beigang, "Band structure of terahertz metallic photonic crystals with high metal filling factor," Appl. Phys. Lett. **92**(20), 201107 (2008).
19. E. I. Smirnova, C. Chen, M. A. Shapiro, J. R. Sirigiri, and R. J. Temkin, "Simulation of photonic band gaps in metal rod lattices for microwave applications," J. Appl. Phys. **91**(3), 960–968 (2002).
20. Y. Zhao and D. R. Grischkowsky, "2-D Terahertz Metallic Photonic Crystals in Parallel-Plate Waveguides," IEEE Trans Microw. Theory **55**(4), 656–663 (2007).
21. A. L. Bingham and D. R. Grischkowsky, "Terahertz 2-D Photonic Crystal Waveguides," IEEE Microw. Wirel. Co. **18**(7), 428–430 (2008).
22. J. Kitagawa, M. Kodama, S. Koya, Y. Nishifuji, D. Armand, and Y. Kadoya, "THz wave propagation in two-dimensional metallic photonic crystal with mechanically tunable photonic-bands," Opt. Express **20**(16), 17271–17280 (2012).
23. Y. Zhang, Y. Xu, C. Tian, Q. Xu, X. Zhang, Y. Li, X. Zhang, J. Han, and W. Zhang, "Terahertz spoof surface-plasmon-polariton subwavelength waveguide," Photon. Res. **6**(1), 18–23 (2018).
24. M. S. Islam, J. Sultana, S. Rana, M. R. Islam, M. Faisal, S. F. Kaijage, and D. Abbott, "Extremely low material loss and dispersion flattened TOPAS based circular porous fiber for long distance terahertz wave transmission," Opt. Fiber Technol. **34**, 6–11 (2017).
25. B. You, T.-A. Liu, J.-L. Peng, C.-L. Pan, and J.-Y. Lu, "A terahertz plastic wire based evanescent field sensor for high sensitivity liquid detection," Opt. Express **17**(23), 20675–20683 (2009).
26. R. Mendis and D. Grischkowsky, "Undistorted guided-wave propagation of subpicosecond terahertz pulses," Opt. Lett. **26**(11), 846–848 (2001).
27. J. W. Lee, T. H. Park, P. Nordlander, and D. M. Mittleman, "Terahertz transmission properties of an individual slit in a thin metallic plate," Opt. Express **17**(15), 12660–12667 (2009).
28. Z. Huang, E. P. J. Parrott, H. Park, H. P. Chan, and E. Pickwell-MacPherson, "High extinction ratio and low transmission loss thin-film terahertz polarizer with a tunable bilayer metal wire-grid structure," Opt. Lett. **39**(4), 793–796 (2014).
29. A. Yariv and P. Yeh, *Photonics* (Oxford University, 2007).
30. B. You, J.-Y. Lu, T.-A. Liu, and J.-L. Peng, "Hybrid terahertz plasmonic waveguide for sensing applications," Opt. Express **21**(18), 21087–21096 (2013).
31. E. Hecht, *Optics* (Addison Wesley, 1998).
32. L. Gingras, M. Georgin, and D. G. Cooke, "Optically induced mode coupling and interference in a terahertz parallel plate waveguide," Opt. Lett. **39**(7), 1807–1810 (2014).
33. C.-J. Wang and L.-Y. Lin, "Nanoscale waveguiding methods," Nanoscale Res. Lett. **2**(5), 219–229 (2007).
34. A. Yariv and P. Yeh, *Photonics* (Oxford University, 2007).

1. Introduction

Photonic crystals (PCs) [1] and waveguide-integrated chips [2] are artificial media which have been extensively developed in optical and terahertz (THz) regimes [3] to manipulate photon transportation and control optical properties by tuning their structural parameters. Various PCs with waveguide integration have been demonstrated for practical use in optical communications [4] and sensing [5]. It is increasingly essential to use THz photons within 0.1–3 THz to probe various chemical compounds and communicate in optical systems for infrared-ray spectroscopy because THz photon energy matches the vibrational or rotational energy-level transitions, related to intermolecular force and molecular dipole moments [6].

In the THz regime, metals are approximated to perfect electric conductors (PECs) to completely reflect THz waves without intrinsic absorption and are thus useful as the low loss waveguide medium. For example, the THz Zenneck surface wave (THz surface plasmon) propagating on a metal sheet performs low waveguide loss, but the guiding field extends

Optics EXPRESS

several millimeters above the metal surface [7]. Some solutions are proposed to control the confinement of THz surface plasmon on a metal surface. One involves fabricating the subwavelength 1D or 2D periodic patterns, called THz spoof surface plasmon polaritons (THz-SSPPs) [8], or coating dielectric layers on the metal surface to reduce the lateral field extension of waveguide modes [9]. Another approach constructs parallel-plate waveguides (PPWGs) with metal-tapered configurations to gradually concentrate the transverse THz field into a subwavelength spatial resolution [10]. However, the SSPP-based periodic structure and PPWG are necessary to integrate the metal plates, dielectric prisms [11] or metal blades [12] to form bulk assemblies for high efficiency excitation of the confined THz waves. It is disadvantageous to the evanescent wave sensing scheme, planar integration with other sensing platforms, and for the development of miniaturized chip systems. When THz surface plasmonic waves propagate without relying on any bulk assembly, the miniaturized waveguide is flexibly compatible with other components on a substrate via the end-to-end or in-line connection.

Recently, integrated THz waveguide sensors based on metal-rod-arrays (MRAs) have been experimentally demonstrated for sensing nano-thin films [13] and liquid drops [14], respectively based on transverse-magnetic (TM) and transverse-electric (TE) polarized wave transmissions. The MRA-guided THz field is phase-sensitive to the analytes both in the TM- and TE-waveguide modes, and the highly sensitive detection of nano-films or liquid drops can be achieved while the waveguide modal field is spatially controlled to match the cross sections of the analytes. This sensing scheme for the MRA waveguide demonstrates the advantages in using the evanescent waveguide field on a miniature chip system. Literatures show that MRA has obvious photonic bandgaps [15, 16] to reject THz waves [17, 18] or microwaves [19], thereby working as artificial media to modulate those waves in PPWGs [20–22]. However, investigation is still needed on THz wave transportation dependent on the geometric parameters of MRA and metal surfaces of periodical rods to reveal the criteria of lateral confinement and low-loss propagation.

In the presentation, the spectral properties and lateral confinement of THz waves guided on the MRA structures are experimentally investigated using THz time-domain spectroscopy (THz-TDS) and compared with theory. From THz transmission spectra, the spectral features of MRA forbidden and transmission bands are demonstrated for tailorable characteristics. Those spectral features can be adjusted from the MRA geometrical parameters in experiments, including the structural periods, metal-rod diameters, interspaces of adjacent metal rods, and propagation lengths for the interactive MRA layer numbers. Because MRA forbidden bands dependent on the structural periods resemble the photonic bandgaps of PC in THz frequency region, the MRA structures are validated as PC-slab waveguides for the transmitted THz waves with lateral confinement in single- and high-order waveguide modes. For the MRA-confined THz waves, the attenuation factors in waveguiding involve the scattering and intrinsic absorption losses, respectively, resulted from the discrete air space among metal rods and the finite metal-rod conductivity at THz frequencies. The propagation loss of the MRA slab-waveguide is mainly contributed by the scattering loss when the metal surface of MRA is ideal as a perfect conductor. Therefore, in theory, an MRA structure constructed using perfect conductive metal rods with a diameter of 0.16 mm and interspace of 0.26 mm can sustain 0.505–0.512 THz waves over a 30 mm propagation length with transmittance above 30%. When the modal fields stabilize after the waveguide propagation above 30 periods of MRA, the single modal power peak is laterally confined on the rod-tips and the propagation scattering loss is only about 0.006 cm^{-1}. Such low waveguide loss and high lateral confinement on the MRA-based PC slab waveguide are superior to the guidance performance of SSPP-based waveguides [23] and the available solid or porous dielectric waveguides [24]. Our results provide valuable information for understanding the relevance between MRA-guided TM waves and waveguide confinement for THz radiation.

Optics EXPRESS

2. Materials and measurement

2.1 Specification of MRA structures

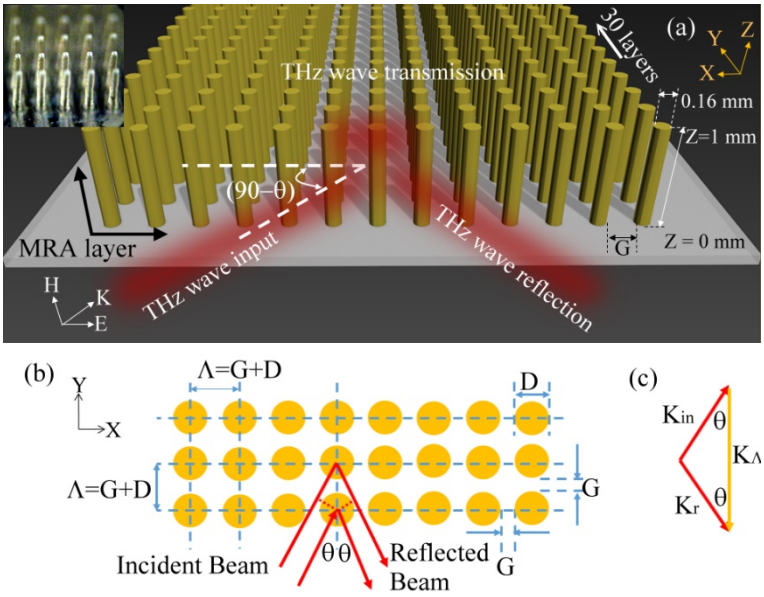

Fig. 1. (a) 3D and (b) top-view schematically drawings for a THz photonic crystal based on an MRA. (Inset) Microscopic photograph of an MRA. (c) Phase-matching diagram of THz wave reflection among metal rods.

As shown in Fig. 1(a), an MRA is composed of multiple rows of one-dimensional rod-array, and each row of MRA lies in the X–Z plane, which is consisted of 13 uniform metal rods with a uniform height of approximately 1 mm. The TM-polarized THz waves can be input at the first row of the MRA with partial transmission and reflection as schematically expressed in Fig. 1(a) for the edge-coupling configuration on a 3D structure of MRA. The 13 metal rods periodically standing in a row are defined as one MRA layer to interact THz waves, which is important to indicate the interactive position and length of MRA along the Y-axis.

In the experiment, different amounts of uniform MRA layer can be precisely fabricated along the Y-axis by micro-stereolithography and sputter-coating methods [13, 14], in which one fabricated MRA is presented in the inset of Fig. 1(a). To investigate geometry-dependent spectral properties of MRA in 0.1–1 THz frequency, the rod diameters of D are controlled at 0.16 and 0.13 mm, and the required interspaces G among the rods are exactly arranged, including 0.26, 0.36, and 0.46 mm. To discuss the interactive length of MRA in THz wave transmission, 30 and 4 layers of MRA are fabricated and compared in the experiment. Furthermore, the high accuracy of micro-stereolithography repeats the 3D structures of rod array, thereby carrying out the comparison between two bare chips with and without metal surface. The fabricated MRAs are measured for THz-wave transmission spectrum using waveguide-based THz time-domain spectroscopy (THz–TDS) [25, 26]. The input spectral range is 0.1–2 THz and the spectral peak is at 0.3 THz with a power signal-to-noise ratio of approximately 10^5.

2.2 Principle of THz photonic bandgap performed in an MRA

The broadband TM-polarized waves passing through a metal slit have been demonstrated and the waveguide modal field exists in 0.1–2 THz that accumulates on and surrounds the metal surface [27]. The TM-waveguide mode of single metal slit can be extended to periodic slits in the MRA layer, thereby having the consistent modal field distribution around the metal

Optics EXPRESS

surface for the large-area illumination of input THz waves [28]. Although the scattering reflectance of broadband TM-waveguide modes is dependent on THz frequency, the waves interfering via the multiple-layer reflection in or outside the metal-rod structure dominates the overall MRA reflection or transmission spectrum. The total scattered THz waves, labeled THz wave reflection in Fig. 1(a), are thus formed by constructively summing up the partially reflected THz waves from several MRA layers along the Y-axis. The MRA interspace G along X- and Y-axes are equidistant but have different contributions in the reflection spectrum. That is, the frequency-dependent reflection of the TM-modal field at one MRA layer is correlated to the X-axial interspace, and the Y-axial interspace can modulate the guided THz waves to perform its characteristic feature in the interference spectrum. Such modulation effect by the Y-axial interspace (or period) of MRA can be explained by the geometries of THz-ray trace [Fig. 1(b)] and THz-wave propagation constant [Fig. 1(c)] as follows.

For THz-ray trace in Fig. 1(b) the path difference of the two reflected THz rays from two adjacent MRA layers is $2\Lambda \cdot \cos\theta$, where Λ and θ are, respectively, the MRA period ($\Lambda = G + D$) and the incident angle. Constructive interference occurs when an integral number of THz wavelengths λ/n_{eff} in the MRA medium fits the path difference. Therefore, the MRA-reflected THz wave follows the equation $2\Lambda \cdot \cos\theta = m \cdot (\lambda/n_{eff})$, where n_{eff} is the effective refractive index and m is an integer. The equation is the so-called Bragg law and effectively predicts the spectral positions of the MRA-reflected THz waves based on a simple geometric path difference [29].

Furthermore, the propagations of the MRA-scattered and incident THz beams obey momentum conservation when the area size of MRA layer is sufficiently larger than that of the input THz beam. The wave vector geometry of the phase-matching condition is described in Fig. 1(c) and represented as $\vec{K}_{in} + \vec{K}_{\Lambda} = \vec{K}_{r}$. $\vec{K}_{in}$ and $\vec{K}_{r}$ are, individually, the propagation constants of input and reflected/scattered waves, which both equal $2\pi n_{eff} v/c_0$. The symbols of n_{eff}, v, and c_0 denote the effective refractive index, THz wave frequency, and speed of light in a vacuum, respectively. $\vec{K}_{\Lambda}$ is an MRA grating wave vector and defined as $2\pi m/\Lambda$, where Λ and m are the grating period and an integer. The MRA-reflected THz waves satisfy the momentum conservation, thereby resulting in serious loss of transmission. Subsequently, serious loss causes spectral dips in a transmission spectrum, namely the photonic bandgaps of an MRA structure to reject THz wave transmission. The center frequency of MRA photonic bandgaps, v_{PC}, can be thus derived and shown as aves

$$v_{PC} = \frac{m \cdot c_0}{2 \cdot n_{eff} \cdot \Lambda \cdot \cos\theta}, \tag{1}$$

which corresponds to the phase-matching condition and equals the Bragg frequency as depicted in Fig. 1(b).

3. Results and discussion

3.1 Period- and interspace-dependent THz photonic bandgaps

With the normal incident condition [i.e., $\theta = 0$ in Fig. 1(a)], the transmission spectra of 0.62, 0.52, and 0.42 mm-Λ MRAs are measured and calculated for the interactive length of 30 layered-MRA and displayed in Figs. 2(a)–2(c). To compare the spectral performances of MRA, we normalize the spectral power peaks individually in measurement and calculation to observe the power ratios at certain frequencies related to the maximum transmission power. The three MRAs indicate different interspaces, namely, 0.46, 0.36 and 0.26 mm, but the same rod diameter of 0.16 mm, individually, for the 0.62, 0.52, and 0.42 mm-Λ MRAs. One obvious rejection band with very low THz transmittance exists in the MRA transmission spectrum, thereby corresponding to the photonic bandgap as explained in section 2.2. The

Optics EXPRESS

measured center frequencies of the photonic bandgaps are 0.258, 0.296 and 0.357 THz, respectively, for the 0.62, 0.52, and 0.42 mm-Λ MRAs, and agree with the first order of Bragg law [m = 1 in Eq. (1)]. The FDTD calculation in a 3D framework reveals that the other high-order Bragg frequencies (m>1) of MRA cannot be found in 0.1–1 THz. The spectral position and bandwidth of MRA photonic bandgap can also be effectively simulated by this numerical calculation to match the measured results, including the blue shift and spectral extension for G reducing from 0.46 to 0.26 mm, as shown in Figs. 2(a)–2(c).

There are two possible factors to hinder high-order Bragg reflection in Figs. 2(a)–2(c). One is the high-order periodical modulation of refractive index along the MRA Y-axis is not realized by the THz beam size, > 1 mm. The other one is the periodical modulation of refractive index along the MRA Y-axis approximates a sinusoidal function because of the X-axial diffraction among the rods, consequently vanishing the high-order Fourier components. In fundamental [29], the periodic index function $n(z)$ in a Fourier series is expressed as, $n(y) = n_0 + [n_1 \Sigma a_m \cdot Exp(-i2\pi y/\Lambda)]$, where n_0 is the spatially averaged refraction index of MRA, n_1 is a constant representing the amplitude of the periodic index modulation and a_m is the m^{th} Fourier component of the periodic index variation. The m^{th} Fourier component along MRA Y-axis has a wavenumber of $m(2\pi/\Lambda)$. Each of the Fourier components, i.e., m, can be considered as an infinite set of partial reflectors with a spacing Λ/m, responsible for a Bragg reflection of order m [Eq. (1)]. To perform the high-order Bragg reflection, the index variation amplitude (a_m) should exist due to suitable modulation geometry and coupling beam size.

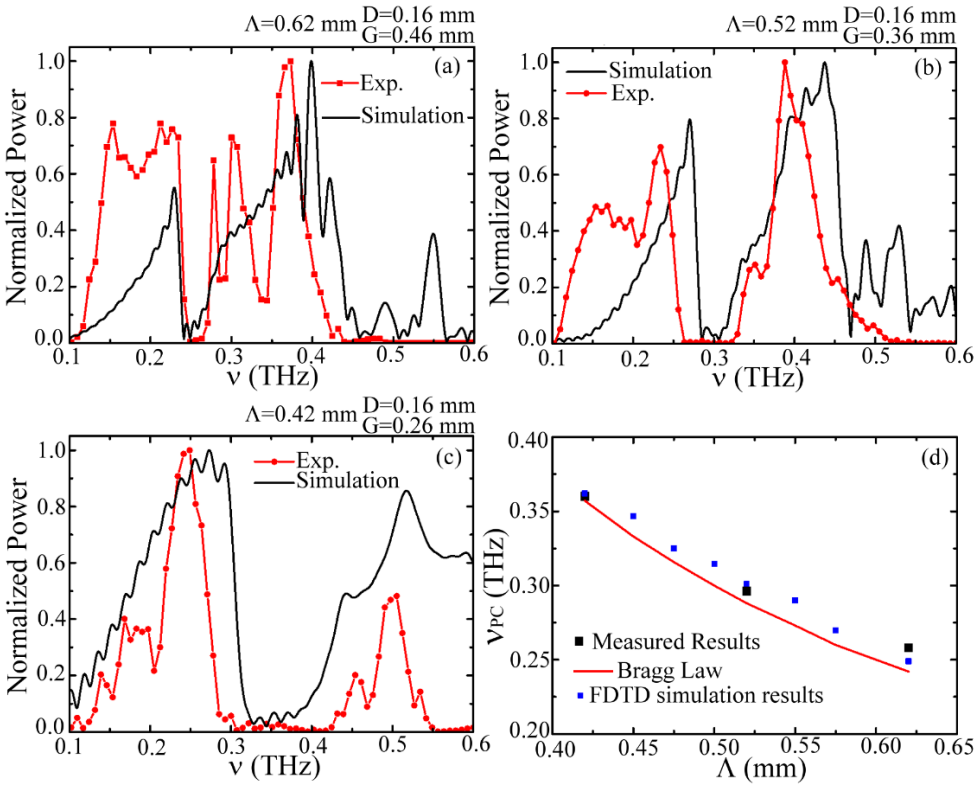

Fig. 2. Theoretical and experimental transmission spectra for the MRAs with different interspaces, (a) 0.46 mm (b) 0.36 mm and (c) 0.26 mm. (d) Theoretical and measured results for the relation between the MRA period and the central frequencies of the photonic bandgaps.

The calculated Bragg frequency based on Eq. (1) with the parameters, D = 0.16 mm, n_{eff} = 1.0, $sin(\pi/2)$ = 1, and m = 1, shows the inverse proportional relation versus Λ as a red line in

Optics EXPRESS

Fig. 2(d). The center frequencies of spectral dips, simulated by FDTD and shown as blue-square dots in Fig. 2(d), indicate the same trend between v_{PC} and Λ, but the FDTD-v_{PC} is slightly higher than Bragg frequency for a certain Λ. The deviation of photonic bandgap frequency between the FDTD simulation and Bragg law is resulted from the input THz beam size approximating to the rod length about 1 mm. In Bragg law [29, 30], the rod length is infinite and the MRA across-section area is much larger than that of THz input beam. FDTD-v_{PC} therefore approximates to the measured value that is expressed as the black-square dots in Fig. 2(d). The v_{PC}-Λ relation indicates that the MRA structure via the edge-coupling configuration can perform as one THz PC with apparent and Λ-dependent photonic bandgaps, whose spectral property follows the first-order Bragg reflection and FDTD simulation of the 3D framework.

The bandwidth of photonic bandgap can be critically controlled by different metal rod diameters for one MRA period. Experimentally, we prepare two MRAs with D values of 0.16 and 0.13 mm within the 0.42 mm Λ to observe THz transmission under the conditions of normal incidence and 30 MRA layers. The measured transmission spectrum of 0.13 mm-D MRA is compared with that of 0.16 mm-D MRA, respectively, as shown by the red-dot and black-dashed lines in Fig. 3(a). The transmitted powers are normalized at the individual spectral peaks to observe the variation of power ratio and bandwidth at photonic bandgaps, in which the normalized transmission spectrum of 0.16 mm-D MRA is applied from Fig. 2(c) as the reference.

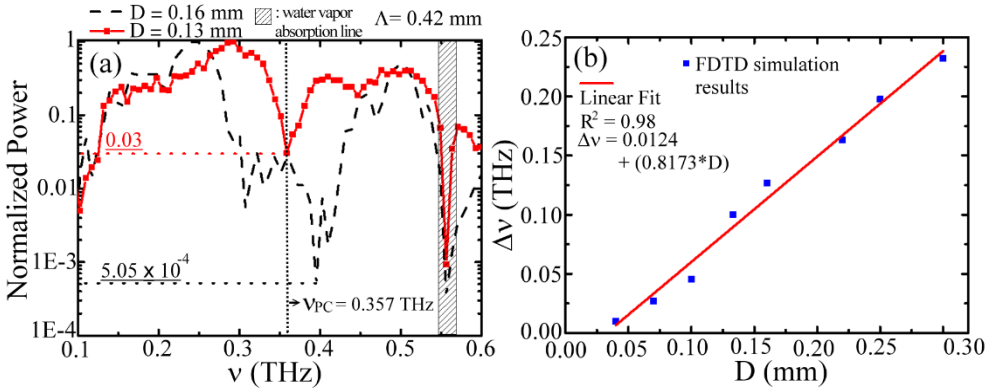

Fig. 3. (a) Transmission spectra of the two MRAs with the same period, 0.42 mm, but different rod diameters. (b) Calculated results for the relation between the metal rod diameter and the bandgap bandwidth based on the same MRA period.

The two MRAs have the coincided center frequency (v_{PC}) of photonic bandgap at 0.357 THz because of the same MRA period, but the bandwidth (Δv) obviously changes when the rod diameter reduces from 0.16 to 0.13 mm. The full width at half maximum of rejection bandwidths for the 0.16 mm- and 0.13 mm-D MRAs are, respectively, 0.202 and 0.04 THz. The result of Fig. 3(a) reveals that the bandgap bandwidth of MRA at a designed PC frequency can be engineered via fine tuning metal-rod diameter. Figure 3(b) summarizes the FDTD simulation result of Δv for various MRA-D values in the same 0.42 mm Λ. The bandwidth proportionally increases with the extension of metal-rod diameter within the 0.42 mm Λ when THz waves normally input and interact with the 30 MRA layers. The proportional relation between D and $\Delta\nu$ is linearly fit with the high R-squared value (i.e., the coefficient of determination in statistics) up to 0.98. The bandwidth responsibility of an MRA photonic bandgap represents that the increase of effective metal cross-section for an MRA PC facilitates THz wave reflection and raises the rejection bandwidth in the transmission spectra.

The power-distinction-ratio, defined as the power contrast between the peak and dip of transmission spectra, obviously reduces as the rod diameter shrinks in a 0.42 mm Λ. Figure

Optics EXPRESS

3(a) presents the spectral dip of 0.42 mm-Λ MRA apparently rises from 5.05×10^{-4} to 0.03 when the metal-rod diameter reduces from 0.16 to 0.13 mm. For shrinking this metal-rod diameter, the corresponding decrement percentage of power-distinction-ratio is around 98%. The reduced metal-rod diameter within a 0.42 mm Λ enlarges the air interspace to decrease THz reflectivity at an MRA layer. Based on the interference theory, the highest visibility of the interference term occurs when the powers of two interference waves are equal [31]. In this case, increasing the D value from 0.13 to 0.16 mm in a 0.42 mm Λ makes the reflected THz wave power via a series of MRA layers approximate to that of the input waves, thereby leading to the increased distinction-ratio or interference visibility at the phase-matching reflection.

3.2 Interactive-length dependent THz wave transmission

In addition to THz reflectivity on each MRA layer, the interactive length between MRA and THz waves also affect the power-distinction-ratio of MRA-PC. Experimentally, we prepare a four-layered MRA to compare with the 30-layered MRA for the power variation of photonic bandgaps in their normalized transmission spectra, in which the geometric parameters of D, G and Λ are respectively 0.16, 0.26 and 0.42 mm. In Fig. 4(a), the measured transmission spectra are illustrated and normalized with the power peaks of approximately 0.25 THz to observe the relative variations of transmission power ratio, where the black-dashed line represents the spectrum of 30-layered MRA and is applied from Fig. 2(c). As expressed in the inset of Fig. 4(a), the relative power level of the spectral dip apparently rises from 5.05×10^{-4} to 2.76×10^{-2} when the MRA interactive length decreases from 30 to 4 layers. The power-distinction-ratio also becomes lower by approximately 98%, near the decreased percentage for reducing metal-rod diameter from 0.16 to 0.13 mm [Fig. 3(a)]. The experiment shows a THz reflection of MRA-rejected waves from the four-layered MRA is certainly less than that from the 30-layered MRA, thus resulting more leaky transmission power in the rejection band of the four-layered MRA. In addition to the photonic bandgaps, the power transmission ratios related to the

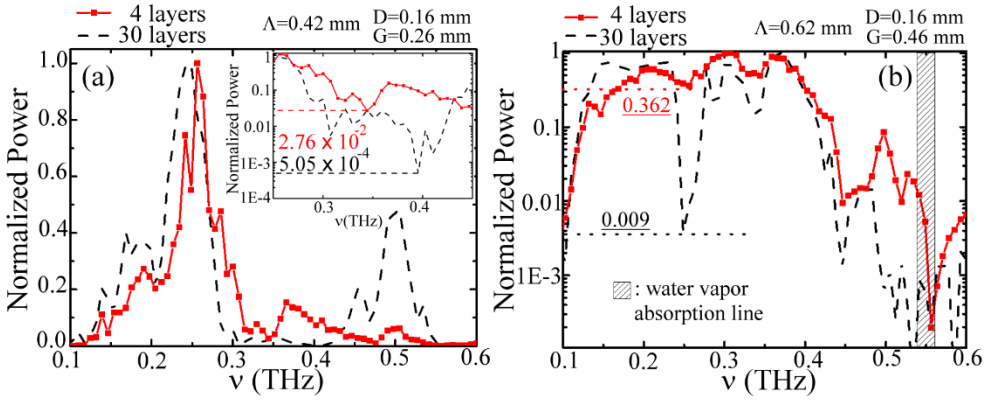

Fig. 4. Normalized power transmission spectra for 4- and 30-MRA layers at different interspaces, (a) G = 0.26 mm and (b) G = 0.46 mm. (Inset) The power levels contrast to the normalized power peak in the rejection bands for G = 0.26 mm.

individual spectral peaks can be modified via the MRA interactive length. In Fig. 4(a), the high-frequency transmission band in 0.42–0.55 THz for the 30 layers of 0.42 mm-Λ MRA possesses a relatively higher power ratio than does the four-layered one. Thus, the 5th up to 30th MRA layers of the 0.42 mm-Λ MRA perform constructive interference to enhance THz transmission at 0.42–0.55 THz. Such constructive interference at high-frequency transmission band is the result of the longitudinal resonance of THz waves among the multiple MRA layers behind the 4th layer.

Optics EXPRESS

When the interspace of an MRA extends larger than 0.26 mm with the same metal rod diameter of 0.16 mm, the rejected waves becomes deliverable along the four-layered MRA and the power–ratio enhancement induced by a 30 layered-interactive length at the high-frequency transmission band is not found. As shown in Fig. 4(b), the spectral power dip of photonic bandgap at 0.258 THz apparently increases from 0.009 to 0.362 when the interactive length reduces from 30 to 4 layers of MRA. For the large interspace, G = 0.46 mm, the enhanced power ratio disappears at the high-frequency transmission band, 0.27–0.40 THz, opposite to the 0.42–0.55 THz waves in the 0.26 mm-G MRA [Fig. 4(a)]. Thus, the leaky THz power through the large gap size, 0.46 mm, is greater than that caused by the constructive interference effect via THz longitudinal resonance among the multiple layers of MRA. By contrast, the enhanced power transmission ratio for the large interspace shifts to the low-frequency band, 0.12–0.24 THz, when the MRA interactive length is increased from 4 to 30 layers.

3.3 Metal-surface dependent THz transmission bands

In addition to the longitudinal resonance inducing the enhanced power transmission ratio, the high-frequency transmission band of 0.26 mm-G (i.e., 0.42 mm-Λ) MRA at 0.42–0.55 THz strongly correlates the metal surface of rod array. Figure 5(a) shows that the polymer-rod-array structure without metal coating (i.e., a bare chip) only passes THz waves in 0.15–0.30 THz, which belongs to the low-frequency transmission band of the 0.42 mm-Λ MRA. The high-frequency transmission band at 0.42–0.55 THz is strongly absorbed by the polymer rods of the bare chip. The reference spectrum of 0.42 mm-Λ MRA, in contrast to the bare-chip spectrum in Fig. 5(a), is applied from Fig. 2(c) and displayed as a black dashed curve.

However, such internal absorption from polymer rods is not so obvious for more extended interspace because more air-space occupation within the THz-wave propagation path benefits THz transmission. The bare chip with polymer rods of 0.16 mm diameter and 0.36 mm interspace is used as an example to compare the transmission spectrum with that of 0.36 mm-G (i.e., 0.52 mm-Λ) MRA in Fig. 5(b). The relative transmission ratios at the high-

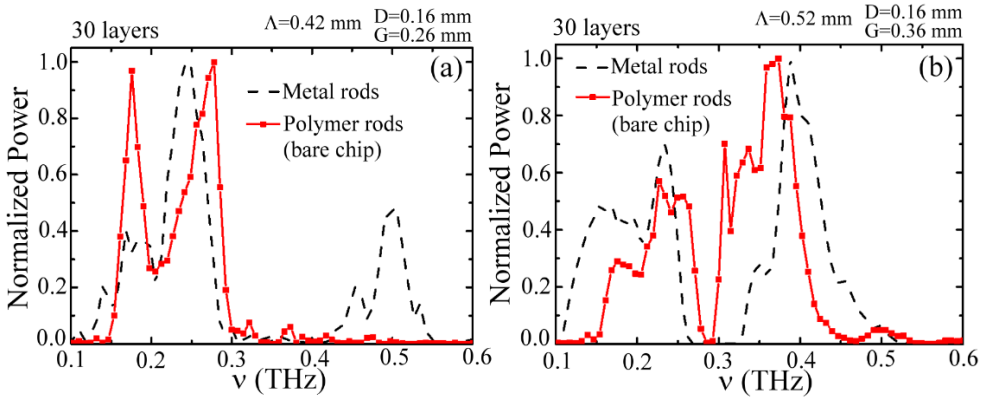

Fig. 5. Transmission spectra of 30-layered MRAs and polymer-rod arrays with the same rod diameter of 0.16 mm and different interspaces of (a) 0.26 mm and (b) 0.36 mm.

and low-frequency transmission bands of the bare chip are similar to those of the 0.36 mm-G MRA, which is depicted as a black dashed curve in Fig. 5(b) and applied from Fig. 2(b). Thus, the high-frequency transmission band of a 0.36 mm-G bare chip is preserved with low THz absorption, opposite to the high transmission loss of 0.26 mm-G bare chip at 0.42–0.55 THz in Fig. 5(a).

Figures 4 and 5 reveal that the enhanced THz transmission based on longitudinal interaction and metal surface along a 30-layered MRA structure is critical to the sufficiently small interspace, consistent with the plasmonic enhancement effect of TM-polarized waves

Optics EXPRESS

inside the metal slits [27]. Experimentally, the MRA geometric parameters for D, G, Λ and MRA-layer plan number, individually, of 0.16, 0.26, 0.42 mm and 30 not only apply to the high power-distinct-ratio on the photonic bandgap at 0.10–0.60 THz, but also as THz plasmonic waveguides with a power ratio enhancement at 0.42–0.55 THz. In the following sections, we further discuss the lateral power confinement and scattering loss for the waves at 0.42–0.55 THz to evaluate the waveguiding ability of MRA.

3.4 Lateral power confinement on metal rod arrays

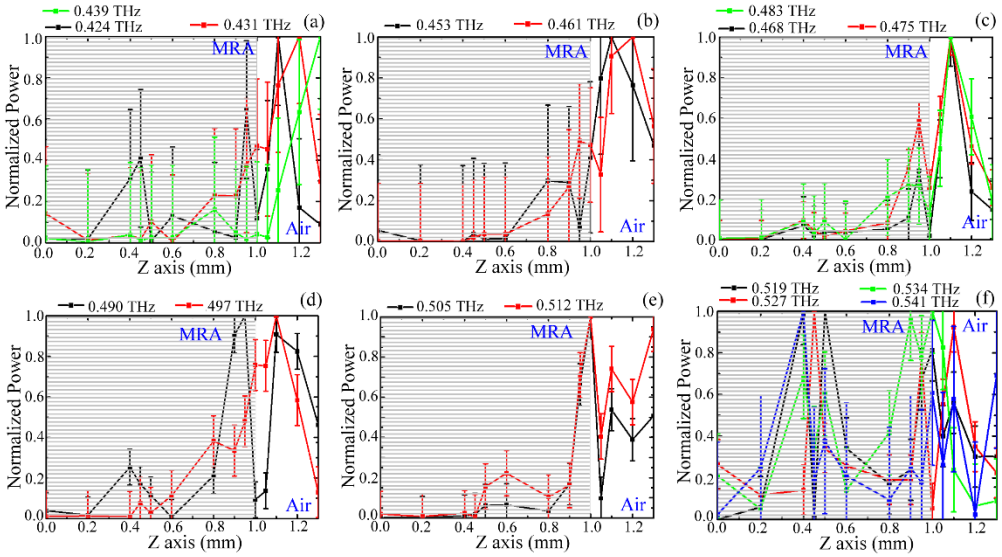

Fig. 6. Measured results for the lateral field distribution along Z-axis at different THz frequency ranges, (a) 0.424–0.439 THz, (b) 0.453–0.461 THz, (c) 0.468–0.483 THz, (d) 0.490–0.497 THz, (e) 0.505–0.512 THz, and (f) 0.519–0.541 THz.

To verify the waves with MRA-enhanced transmission in 0.42–0.55 THz and inside the 0.42 mm-Λ MRA structure (G = 0.26 mm, D = 0.16 mm) as waveguide modes, their lateral power distributions along the Z-axis (i.e., rod axis) should be observed. Experimentally, the integral waveguide powers from Z = 0 to 1.3 mm at the 30th layer of MRA (i.e., output end) are measured by the knife-edge method and differentiated to observe modal power distributions at different Z-axial positions, which are normalized at individual maximum powers and illustrated in Figs. 6(a)–6(f). The knife-edge position at Z = 1.3 mm is sufficiently large to pass all THz wave power in 0.42–0.55 THz, and all the power is contrarily blocked for Z = 0 mm. The metal thickness of knife-edge is less than 0.1 mm, much smaller than the wavelengths of THz waves in 0.42–0.55 THz, and a blade attached on the output-end rod surface is workable for the open frame structure of an MRA. Therefore, the wave interference between the interfaces of knife-edge and MRA layer does not occur [32]. Furthermore, the measurement deviation, presented as the error bars in Fig. 6, were obtained from three rounds of THz-waveform measurement at different Z-axial positions, 0–1.3 mm. For the same THz waveform measurement, the power fluctuation at 0.424–0.453 and 0.534–0.541 THz frequencies is about +/–30% but reduces to +/–10% at 0.461–0.527 THz with relatively high amplitude. The spectral powers at these three frequency ranges are derived from the same THz waveform without manual deviation to tune THz frequency. Although the power fluctuation at the spectral edge is higher than that of the spectral center for a measured THz-waveform, the frequency-dependent power response at any position of Z-axis is distinct to discuss due to the statistical analysis on three THz waveforms at each Z-axis position.

In Fig. 6(a), 0.424 THz wave at the spectral edge of high-frequency transmission band [Fig. 2(c)] performs multiple power peaks along the Z-axis at 0.4, 0.9 and 1.1 mm, thereby

Optics EXPRESS

corresponding to a high-order waveguide mode in the Z-axis. However, the waves with 0.431 and 0.439 THz frequencies have single power peaks in Z-axis because their related power ratios for the knife-edge positions at Z = 0.4, 0.9 and 1.1 mm are lower than that of 0.424 THz wave. Thereby, the two waves perform the single Z-axial waveguide modes and spread in the air cladding apart from the rod-tip surface at approximately 0.2 mm (i.e., Z = 1.2 mm). Here, the rod-tip surface is the X–Y plane at Z = 1.0 mm and called as MRA-tip surface. When THz frequency rises to 0.453–0.483 THz as shown in Figs. 6(b) and 6(c), the Z-axial modal power peaks are closer to the MRA-tip surface, compared with those of 0.431 and 0.439 THz waves. The 0.490 and 0.497 THz waves near the high-frequency transmission peaks have relatively high fractions of power inside the MRA structure, as illustrated in Fig. 6(d) and are compared with those low-frequency waves in Figs. 6(a)–6(c). However, the modal power peaks of 0.490 and 0.497 THz waves remain outside the MRA, Z = 1.1 mm. For the waves at 0.505 and 0.512 THz frequencies, the lateral power confinement as shown in Fig. 6(e) is better than that of 0.490 or 0.497 THz wave [Fig. 6(d)] because their Z-axial power peaks are approximately located at the MRA-tip surface. Such MRA-guided THz waves on the metal-rod tips are equivalent to

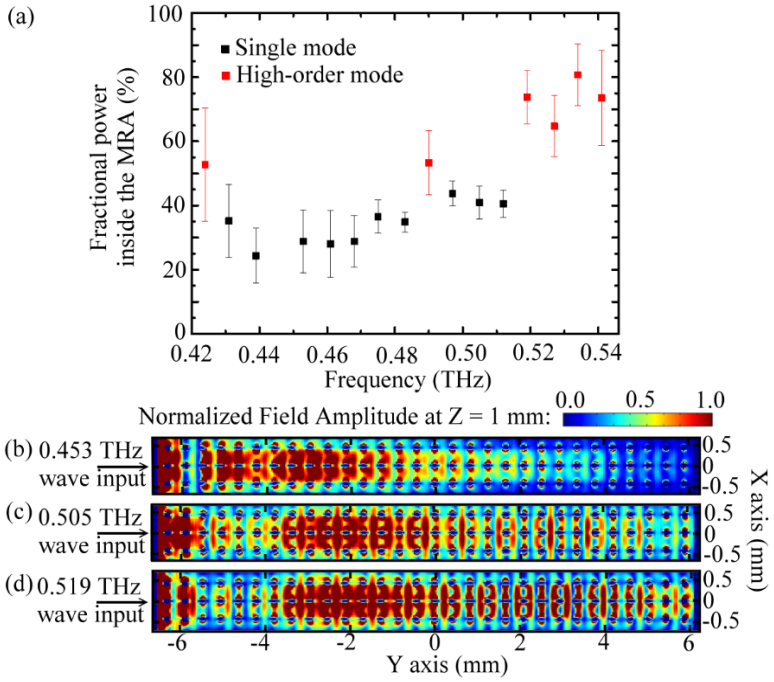

Fig. 7. (a) Measured power fractions inside the MRA for the single and high-order modes along the metal rod axis. Simulated electric field distributions in the X–Y plane at Z = 1.0 mm for different THz frequencies: (b) 0.453 THz, (c) 0.505 THz, and (d) 0.519 THz.

surface-confined fields at the air-MRA interface, thereby resembling the plasmonic waveguide schemes [33]. When THz wave frequency rises to 0.519–0.541 THz, the surface-confined power peaks split partial power inside the MRA structure. As shown in Fig. 6(f), the 0.519–0.541 THz waves have two Z-axial power peaks, respectively, at Z = 1.0 and 0.4–0.5 mm, thereby corresponding to the high-order waveguide modes in the Z-axis, and are considerably confined, as opposed to the loosely confined high-order modes at 0.424 and 0.490 THz [Figs. 6(a) and 6(d)].

Based on the measured results in Fig. 6, the fractional power of waveguide mode inside the MRA is further estimated in Fig. 7(a) for the Z-axial single and high-order modes, respectively, denoted as the black- and red-square dots. The related error bars are estimated

Optics EXPRESS

from the power fluctuation at Z-axial position of 1 mm for the repeated measurement of THz waveforms. The high-order modes occur at 0.424, 0.490, and 0.519–0.541 THz. The single modes lie at 0.431–0.483 and 0.497–0.512 THz. Obviously, the high-order modes indicate a power fraction range of 53–81%, which is considerably higher than that of the single modes at 24–44%. For frequency increased from 0.42 to 0.55 THz as shown in Fig. 7(a), the power fraction value inside the MRA slightly increases with THz frequency both for single and high-order modes, thereby approximating the frequency-dependent confinement of a dielectric slab waveguide [34].

Three waves at 0.453, 0.505, and 0.519 THz frequencies are then used as examples in FDTD calculation to observe the modal field distributions on the MRA-tip surface, which are individually shown in Figs. 7(b)–7(d). The 0.453 THz field as shown in Fig. 7(b) is seriously decayed with propagation length and not confined overall at the MRA-tip surface because the Z-axial power peak is outside the surface, as shown in Fig. 6(b). Figures 7(c) and 7(d), respectively, show 0.505 and 0.519 THz waves cover all the 30 layers of MRA, thereby representing that their lateral fields are well confined at the tip surface and consistent with the lateral power peaks measured at the rod tips of the output end [Figs. 6(e) and 6(f)]. The simulated electric field distributions on the MRA-tip surface along the wave propagation direction show the loosely confined THz waves, such as the 0.453 THz wave, with Z-axial power peaks above the rod tips, cannot propagate for a long length of MRA. However, the waves of 0.505–0.541 THz with modal power peaks at the rod tips, including the single- and high-order modes, are effectively confined to propagate for relatively long propagation lengths. It represents that the TM-waveguide modes within the X-axial interspace of 0.26 mm and at 0.505–0.541 THz frequency can be experimentally confined inside the 1 mm-thick MRA for the 30-layer propagation, which is dependent on the critical factors of MRA-layer number, interspace, or reflectivity as shown in Figs. 4 and 5.

3.5 Scattering loss of MRA waveguide

To observe THz scattering loss of the MRA-enhanced waves in 0.42–0.55 THz and along the 0.42 mm-Λ MRA (G = 0.26 mm, D = 0.16 mm), the transmittance after different layers of MRA are calculated based on the perfect-conductive rods (i.e., PEC) and shown in Fig. 8(a). The transmittance of 40–85 layered MRA is apparently lower than that of the 20 or 30 layered MRA because some percentages of MRA-guided power radiate or scatter out of the rod-array structure without being confined by the MRA interspace. For 0.42–0.55 THz waves, their modal power distributions in the X–Z plane are almost fixed when waveguide length is longer than 30 layers but the transmittance performs an exponential decay between the 30th and 85th layers of MRA. The trend of transmittance decay with the structural length is consistent to the waveguiding performance in the dielectric or metal plasmonic media.

We take the three waves at 0.453, 0.505, and 0.519 THz as the examples to analyze their FDTD transmittances versus MRA-waveguide lengths in Figs. 8(b)–8(d). The X–Z modal field distributions at the 30th MRA layer are also calculated and shown at the insets of Figs. 8(b)–8(d). These three waves following the comparison in Figs. 6 and 7 indicate different Z-axial modal power distributions at the output end (Fig. 6) and the corresponding confinement abilities on the MRA-tip surface (Fig. 7). The modal fields shown in the insets of Figs. 8(b)–8(d) are the TM-polarized waveguide modes inside the periodic interspaces because the fields, accumulating on the metal rod surface and extending to the interspace between adjacent metal rods, are almost consistent with those observed in the single metal slits [27]. The transmittance variations of 0.453, 0.505 and 0.519 THz-waves along the length longer than 20 MRA layers are apparently different and strictly relate to the lateral confinement capability of the MRA waveguide modes in Z-axis. That is, 0.453 THz wave has the modal power peak outside the MRA-tip surface, and the transmittance is considerably low with obvious variation between 40 and 85 layers of MRA. In the same propagation range, 0.505 and 0.519 THz waves have higher transmittance, > 30%, and smaller variation range of

Optics EXPRESS

transmittance because of the higher lateral confinement, which is compared with that of 0.453 THz wave in Figs. 6 and 7 and the insets of Fig. 8.

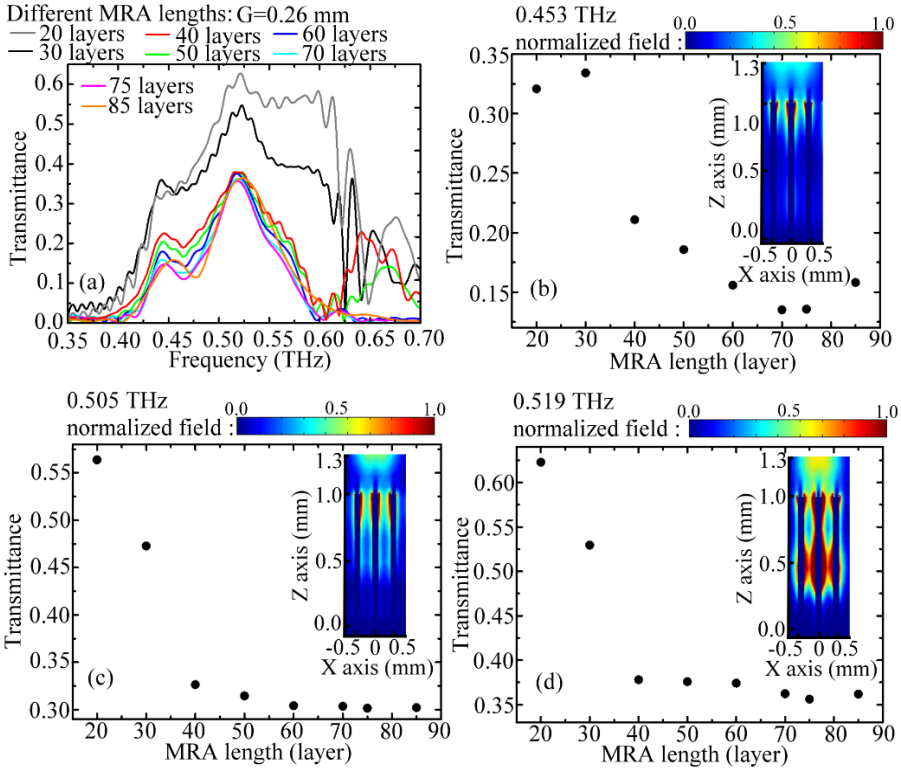

Fig. 8. (a) Calculated transmittance spectra for THz waves propagating after different lengths of MRA. Calculated THz transmittances of (b) 0.453 THz, (c) 0.505 THz, and (d) 0.519 THz waves for different waveguide lengths, where the insets show the electric field distributions in the X–Z plane at the 30th layers of MRA.

Based on the transmittance spectra in Fig. 8(a), the scattering loss in 0.42–0.55 THz at different waveguide intervals are consequently summarized in Fig. 9. We define that the output power of a certain length of MRA, $P_{1,\,2}$, equals $P_0 \cdot \tau_{1,\,2}$, where P_0 and $\tau_{1,\,2}$ are respectively the input power and the transmittance through an MRA length, $L_{1,2}$. The length L_1 is shorter than L_2 and the corresponding transmittance τ_1 is larger than τ_2. Therefore, the output power of L_2-MRA length is, $P_2 = P_0 \cdot \tau_2 = P_1 \cdot exp[-\alpha \cdot (L_2 - L_1)] = P_0 \cdot \tau_1 \cdot exp[-\alpha \cdot (L_2 - L_1)]$, and the equation can be summarized as, $ln(\tau_1/\tau_2) = \alpha \cdot L$, where $L = (L_2 - L_1)$ and α are respectively the MRA interval and scattering loss coefficient. The scattering loss of Fig. 9 is consequently obtained from the equation, $\alpha = ln(\tau_1/\tau_2)/L$, when we consider the 10 layers of MRA, 0.395 cm, as the interval L. Figure 9 shows the highest scattering loss occurs in the interval of 30–40 MRA layers. However, the TM waveguide modal field along the Z-axis are not fixed to exist on the metal rods between the 20th and 30th layers of MRA; so that, the scattering loss of certain waves in 0.42–0.46 THz cannot be reasonably obtained at the interval of 20–30 layers, which is presented as the dashed line in Fig. 9. When the waveguide length of MRA is longer than 50 layers, the scattering loss values are stabilized, and the lowest values occur at 0.505 and 0.519 THz, respectively, around 0.006 and 0.003 cm^{-1}. These two values are, respectively, the single- and high-order waveguide modes in the Z-axis [Figs. 6(e) and 6(f)]. Although the propagation length of MRA should be sufficiently long to perform the stable waveguide loss, the longitudinal resonance along the Y-axis still occurs,

Optics EXPRESS

thereby resulting in the obvious fluctuation of scattering loss for certain frequency ranges at each interval [Fig. 9].

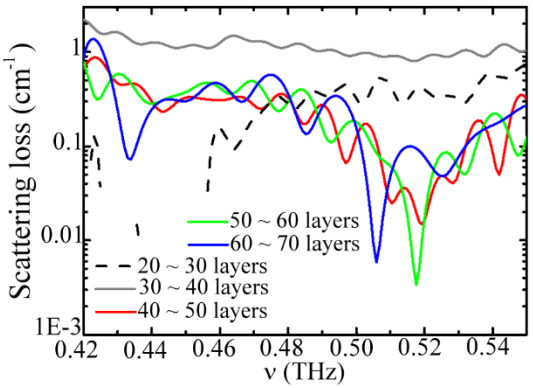

Fig. 9. Calculated THz scattering loss of MRA at different waveguide intervals.

4. Conclusion

Laterally confined THz wave guidance is experimentally demonstrated on a 1 mm-thick planar waveguide composed of MRA, and the spectral properties of the MRA-based waveguide are comprehensively investigated by using THz transmission spectroscopy and compared with theory. An MRA structure is characterized as one THz-PC waveguide, spatially modulating and strongly reflecting THz waves to form one photonic bandgap at 0.10–0.60 THz. The photonic bandgap of an MRA-PC waveguide can be manipulated by changing the MRA geometry parameters and is effectively consistent between experiment and FDTD simulation. Increasing the rod diameter and layer number of an MRA structure or decreasing the interspace between adjacent rods obviously increases the spectral width and power distinction (i.e., visibility) of the stop band because the reflectivity of each MRA layer rises to facilitate constructive interference of THz reflection. The power ratio enhancement relating to a spectral peak value for the measured transmission band of 30-layered MRA PC waveguide is verified because of longitudinally resonant guidance of TM-polarized waveguide modes along the MRA length, which is critical to the interspace width of adjacent rods and the metal coating of rod surface. An MRA slab waveguide is further validated to guide both single- and high-order modes along the rod axis (or Z-axis) with different propagation losses. Single waveguide modes of an MRA structure can propagate for long distances with low scattering loss and indicate lateral confinement with power peak at MRA-tip surface because the fractions of modal power inside the MRA slab waveguide are relatively lower than those of the high-order modes. For example, the highest transmission power of a 30-layered MRA waveguide with a 0.26 mm *G* and a 0.16 mm *D* occurs at around 0.505–0.512 THz. Such MRA-guided THz waves in this frequency range (0.505–0.512 THz) are experimentally and theoretically demonstrated as single-mode guidance with modal power peaks laterally confined on the metal rod tips and the corresponding fractional power inside MRA is approximately 40%. Based on the ideal PEC assumption, 0.505–0.512 THz waves indicate extremely low scattering loss, 0.003 cm^{-1}, and propagate for a long distance over 30 mm with the transmittance above 30%.

Funding

Ministry of Science and Technology of Taiwan (MOST 104-2221-E-006-163-MY3).

Optics EXPRESS

Acknowledgment

This work was supported by grants-in-aid for scientific research from the Ministry of Science and Technology of Taiwan (MOST104-2221-E-006-163-MY3), Japan Society for the Promotion of Science (JSPS, KAKENHI, JP17K45678) and Bureau of Standards, Metrology and Inspection of the Republic of China (Taiwan).